

# Optical Sensing and Control Methods for Soft Pneumatically Actuated Robotic Manipulators

Jennifer L. Molnar, *Student Member, IEEE*, Ching-An Cheng, *Student Member, IEEE*, Lucas O. Tiziani, Byron Boots, *Member, IEEE*, and Frank L. Hammond III, *Member, IEEE*

**Abstract**– A low-cost optical sensing method for improved measurement and control of soft pneumatic manipulator motion is presented. The core of a soft continuum robot is embedded with several optically-diffuse elastomer sensors which attenuate light depending on their strain mode and degree. The optical sensors measure local strains at the robot’s axial center, and these strain data are combined with measured actuator chamber pressures to determine the pose of the robot under various gravitational and tip loading conditions. Regression analyses using neural networks (NNs) demonstrate that when the soft continuum robot’s base orientation is fixed, the position of its end-effector can be estimated with 3.42 times more accuracy (71% smaller root mean squared error) when using both optical sensor and pressure data (~2.44mm) than when using only pressure data (~8.3mm). When the robot’s base orientation was varied, the combined optical sensor and pressure data provide position estimates which are as much as 37.8 times more accurate (~2.76mm) than pressure data alone (~104mm).

## I. INTRODUCTION

The compliant nature of soft robots enables them to perform functions that are difficult for more traditional, rigid-body robots to accomplish, such as adaptive locomotion in tight spaces [1, 2], and safe movement in close proximity to, or in direct contact with, human beings [3-5]. Effective utilization of these capabilities requires advanced modeling techniques and control strategies which can accommodate the continuous, often non-linear deformations of these flexible devices [6]. The accuracy and utility of many modeling methods and control strategies are often dependent on the availability of real-time kinematic information, which itself requires 1) a sensing method which is precise and can span large motion ranges and 2) a robust method of estimating robot poses from that sensor data.

**Critical Challenge:** Recent work [7, 8] on the design and control of soft inflatable continuum robots demonstrates how well the kinematic states of such devices can be estimated with proper mechanistic models and pressure sensing. This work, however, also highlights the challenges of soft robot

Manuscript received on September 15, 2017. J. Molnar and L. Tiziani are with the Adaptive Robotic Manipulation Laboratory, Woodruff School of Mechanical Engineering, Georgia Institute of Technology.

C.-A. Cheng and B. Boots are with the School of Interactive Computing within the College of Computing at Georgia Tech.

F. L. Hammond III is with the Adaptive Robotic Manipulation Laboratory, Woodruff School of Mechanical and the Coulter Department of Biomedical Engineering, Georgia Institute of Technology, 313 Ferst Drive NW, Atlanta, GA 30332, USA (email: [frank.hammond@me.gatech.edu](mailto:frank.hammond@me.gatech.edu)).

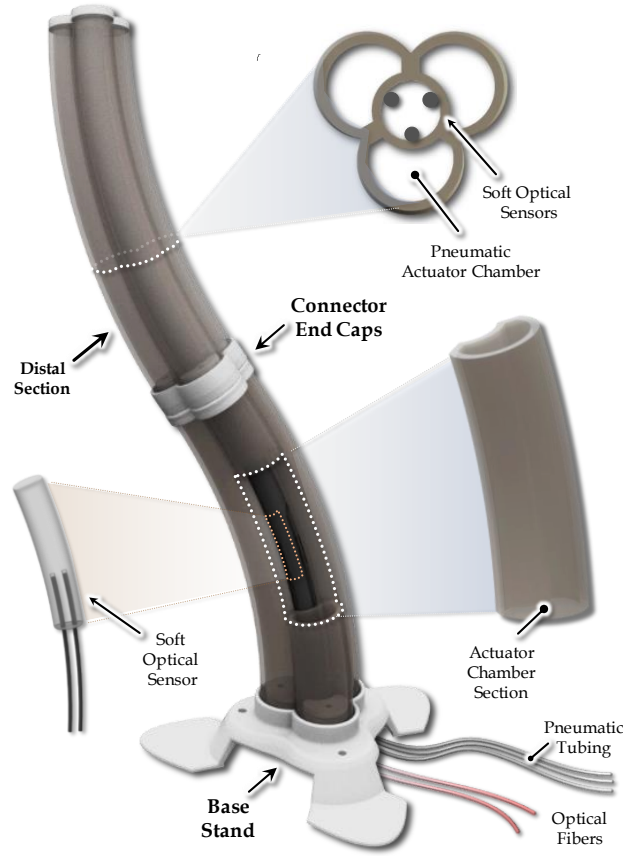


Figure 1. Rendering of a soft, pneumatically-actuated continuum robot with an optical sensor-embedded core for position sensing.

control when such devices are under external loading or exposed to unexpected mechanical disturbances [9]. These challenges are exacerbated further by the use of compressible fluidic actuation media (gasses) which complicate system dynamics and demand special control considerations.

**Current Solutions:** As with many multi degree of freedom (DoF) systems having complex state-spaces, control accuracy can be improved by augmenting sensing capabilities. Adding sensors to soft robots helps achieve greater controllability, but the type of sensor must be selected carefully to ensure manufacturing feasibility and device function. Several common sensing modalities and methods have been used in soft robotics, each having unique benefits and drawbacks.

- *Feature and fiducial-based tracking* methods such as visual servoing and electromagnetic (EM) sensing have been used to monitor the deformation of soft robot bodies, and have the advantage of ease and versatility in implementation (i.e. placement of cameras and trackers). However, they also suffer from susceptibility to visual occlusions and electromagnetic interference [10].
- *Mechanical sensors* used for actuation and control, such as pressure/barometric sensors (pneumatic systems) and cable encoders (tendon-driven systems), are precise, reliable, and can provide explicit, easy-to-interpret information on mechanical changes in soft systems. These sensors, however, generally require special mechanical design considerations to ensure that the large, complex deformations of soft robots can be captured. The influence of external forces in particular (e.g. gravitational loading or contact with an object in the environment) may be largely invisible to these sensors [7].
- *Soft strain sensors* are perhaps the most promising solution to soft robot control as they can be fabricated from the same material as the soft machines and, therefore, undergo the same modes of mechanical strain. Examples of such sensors include conductive liquid embedded sensors (most commonly eGaIn sensors) [11], FBG sensors [12], macrobend optical waveguide sensors [13], and optically transparent silicone waveguides [14, 15]. While many of the soft sensors reported in literature demonstrate high accuracy, robustness against disturbances (e.g. undesired off-axis deformations), and reliability in practice, the fabrication processes and signal conditioning hardware required can make distributed sensing approaches, with large numbers of embedded sensors, challenging.

Our objective in this work is to utilize soft diffractive optical sensors, recently developed by our group, to measure mechanical strain in a soft, pneumatically actuated continuum robot [16]. These sensors are similar to the aforementioned silicone waveguide sensors [14, 15], but utilize optically diffractive microparticles within the sensor body to facilitate light transmission from transmitter to receiver. This partially linearizes the bending response curve, while also requiring only co-located optical fiber pairs at the site of strain measurement (one for light emission, the other for light detection). The light emitter and detector hardware can be located away from the measurement site, eliminating the need for any rigid or metallic components on-board the soft devices. The diffractive optical sensors may also be fabricated as part of the native soft material of the device, making distributed sensing feasible. We aim to demonstrate that this technology can provide a low-cost, viable solution to distributed sensing on soft robots which can improve our ability to measure their complex motions and loading conditions and, thereby, enable greater controllability.

As a proof of concept for distributed soft optical sensing, we embed a set of such sensors at the center of the continuum robot to measure complex deformations over various pneumatic actuation and loading conditions. Section II describes the design concept and fabrication of the soft,

optical sensor-embedded continuum robot. Section III details the experimental evaluation of the robot, and Section V explains analysis methods, in particular neural networks (NNs), used on the experimental data. Sections V and VI discuss insights gleaned from the results and future work, respectively.

## II. DESIGN METHODOLOGY

The soft continuum robot used in this work is comprised of the major components: fiber-reinforced pneumatic actuators, a pneumatic control system, and a soft optical sensing system (Fig. 1). The following describes the design and fabrication method for each system component.

### A. Robot body fabrication

Our robot design and fabrication process is similar to that described in a previous work by Marchese and Rus [7]. This design involves a multi-step casting process to create a set of slightly-tapered, fiber-reinforced chambers. These are equally spaced around a hollow central core, through which pneumatic tubes and sensor leads may be passed. Our design involves three pneumatically-actuated chambers, rather than the common four or six associated with more redundantly-actuated designs [17]. This configuration allows for bending of the robot in all directions and, if inflated or deflated concurrently, controlled extension or contraction.

The actuator chambers are hollow, with 3mm thick walls on all sides, to permit maximal expansion of each actuator and minimal resistance of the silicone on the opposing side. Sections may be combined end-to-end through the use of 3D printed locking end pieces, with pneumatic tubing for inflating distal sections contained within the hollow core of lower segments. In this work, we focus our testing and analysis on a single soft continuum robot segment (Fig. 2).

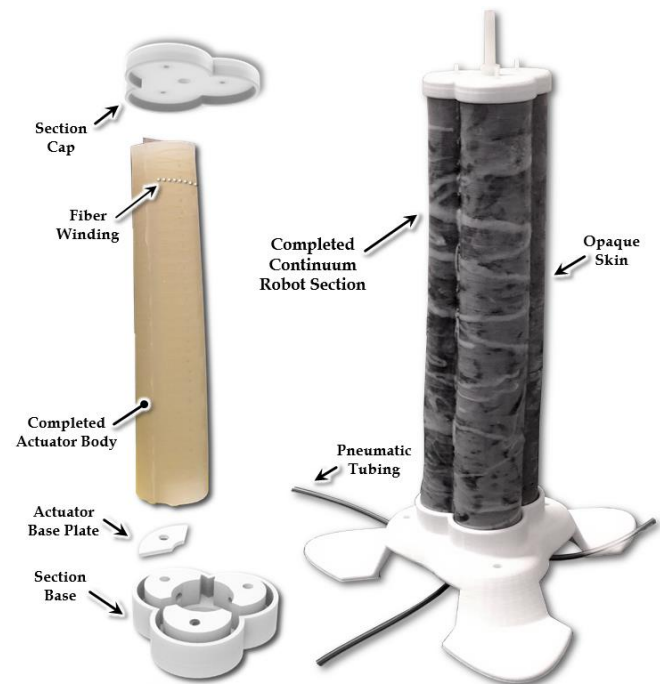


Figure 2. The design of the individual soft pneumatic actuator (left) and the assembled soft continuum robot section, comprised of three actuators.

For fabrication, individual chambers were first cast between a 3D-printed plug (Fablicator, KL Services Group, Inc.) and a 2-piece external mold (for ease of removal). This initial casting was done using DragonSkin10 silicone (Smooth-On), and was 2mm thick. The outer mold was removed and each chamber was wrapped with a Kevlar thread (McMaster-Carr) in a crossed helical pattern, with windings spaced 5mm apart [8, 18]. The three chambers were inserted into an encapsulation mold with a 1mm margin and another plug to ensure a hollow core. This margin was filled with opaque gray EcoFlex50 to provide an optical shield for the core while simultaneously joining all chambers together.

The actuator assembly was placed over a 3D-printed base, and pneumatic tubing (semi-clear rubber silicone, 1/8" ID) was fed into each chamber through holes in the base. Silicone (Ecoflex50, Smooth-On Inc.) was injected via syringe inside the chamber to seal off any leaking areas (Fig. 2). Thin plastic plates, printed to fit inside the interior of the distal end of the chamber, were inserted into the tip of each chamber through slots cut near the top. These provided anchors for screws which passed through the silicone end of the robot body and held the end cap in place. Ecoflex50 silicone was injected via syringe into the distal end of each chamber to seal up the slot, screw hole, and any other potential leaks.

### B. Sensor Fabrication

The soft optical sensors are based upon previous work [16], where we placed optically-refractive microspheres in otherwise clear silicone. The resulting optical properties change in response to deformation and can be used to monitor strain, pressure, and/or bending information about the sensor body. A co-located optical sensor model was implemented to ease fiber optic routing; all electrical components, including infrared LEDs and photodiodes, were located near the base of the robot. Sensors were placed along the inner core and secured next to each chamber. This location was selected to ensure that these optical sensors were more likely to undergo linear and bending strains, with little to no deformation due to internal pressures generated by inflation of the pneumatic actuators.

To construct the sensors, optically-clear silicone (SortaClear18, Smooth-On Inc.) was mixed with glass microspheres (3M Glass Bubbles, 3M, Inc.) in a 20:1 ratio by volume. This mixture was injected into 3D-printed cylindrical molds (Fablicator, KL Services Group, Inc.) 5mm in diameter and 20mm long. Small holes on either end of the mold provided guides for inserting two piano wires lengthwise through the body of the sensor. After curing, these wires were removed, providing the space for polished 0.75mm diameter unjacketed fiber optic cables (Fiber Optic Products, Inc.) to be inserted (Fig. 3).

The fiber optic strands were inserted 10mm into the sensor and secured on the outside with silicone adhesive (Sil-Poxy, Smooth-On, Inc.). More of the microsphere-filled silicone was injected via syringe at the opposite side of the sensor, to fill in the rest of the channel left by the wire and to further secure the optical fiber in place. The floating ends of the optic cable were then attached to an IR emitter (SFH-4350, OSRAM Opto Semiconductors, Inc.) and an IR photodiode in

a screw-tight, connector-less package (IF-D91, Industrial Fiber Optics, Inc.). Signal response proved to be dependent on fiber alignment at the emitter/photodiode juncture, so ends were firmly secured by using electrical tape to create a tighter fit in the screw-tight photodiode housing and the custom 3D-printed IR emitter housing (Fig. 3).

For sensor strain testing, the IR emitter was powered at 1.4V using a 0.08A current-limited external power supply. The sensor was attached to an Instron 5540 Series system (Instron Inc., USA) using alligator clips, which clamped onto the leads at one end (covered with electrical tape for protection) and a bead of Silpoxy attached to the tip of the other. The set-up was shielded from ambient light by a draped sheet of black-pigmented silicone (Silc-Pig, Smooth-On, Inc.). The Instron extension profile began with the sensor positioned vertically, under low tension; the heads pulled

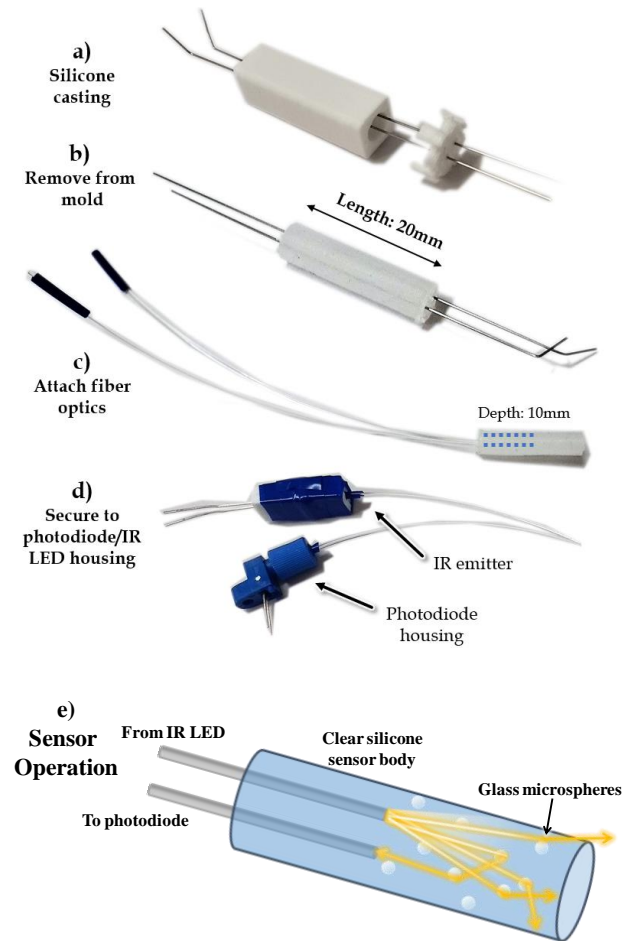


Figure 3. Sensor fabrication process. a) 20:1 mixture of SortaClear18 silicone (Smooth-on Inc.) and glass microspheres (3M Glass Bubbles, 3M, Inc.) is poured into a 3D-printed mold 5mm in diameter and 20mm long. Two pieces of piano wire are inserted to form parallel, hollow guide channels. b) Silicone sensor body is removed from the mold. c) Piano wires are extracted and 0.75mm fiber optics (Fiber Optic Products, Inc.) are inserted to a depth of 10mm. More silicone mixture is injected via syringe from the other end of the sensor to fill in any remaining gaps and secure the fiber optics in place. Ends of fiber optics are wrapped in electrical tape for more secure fitting in photodiode/LED housing. e) Sensor operates by detecting light transmission between the two optical fibers inside the silicone. When the sensor is attached to the wall of an actuator, the sensor body stretches with the chamber wall, causing the glass microspheres to spread apart and reflect less light back to the photodiode.

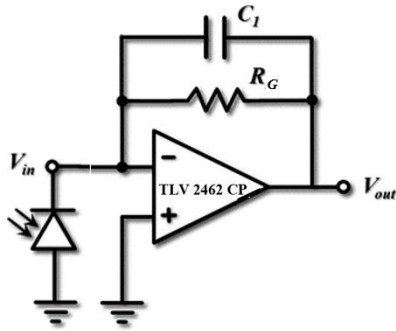


Figure 4. Transimpedance amplification circuit, with  $R_G = 20 \text{ M}\Omega$ ,  $C_1 = 1 \text{ nF}$ .  $V_{in}$  is the output of the photodiode.

away from each other at a rate of 0.1mm/s to a distance of 10mm (elongation: 150%) before returning. Twenty cycles of extension were run, with the photodiode current being channeled through a transimpedance amplifier (Fig. 4) to where it was recorded by a National Instruments myDAQ. The gain resistor for the amplifier was hand-tuned using resistors between 5-100  $\text{M}\Omega$ ; the sensor used for the strain test had adequate response levels at 20 $\text{M}\Omega$ .

The voltage-strain response can be seen in Fig. 5. Voltage increases monotonically with strain, and demonstrates reasonable consistency after the initial few cycles. During this “breaking in” period, the stiff optical fibers shifted within the silicone body of the sensor as the sensor body was extended and did not fully return upon release. After three cycles, the sensor reached a steady-state position between silicone and fiber, and the voltage response stabilized.

Finally, three optical sensors were attached with SilPoxy to the inner core of the continuum robot at a height of 15 cm from the base. Sensors were oriented vertically, one per

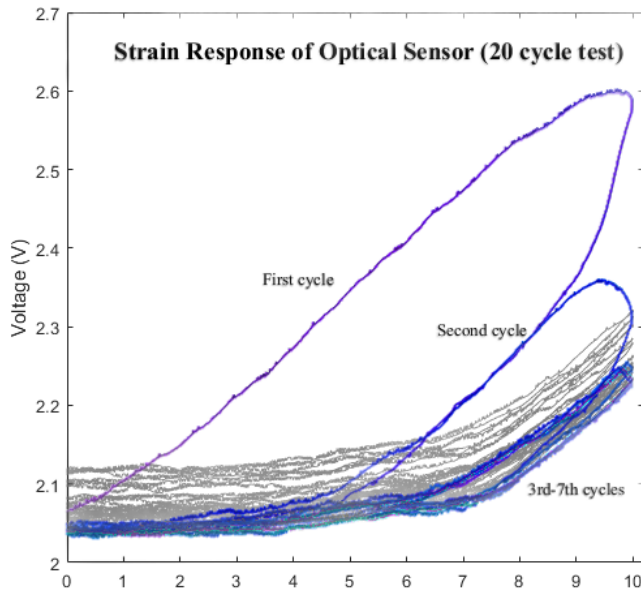


Figure 5. Voltage response of optical sensor while being elongated from 10 to 20mm. Initial strain cycles show a large amount of hysteresis, caused by the stiff optical fibers shifting within the silicone body of the sensor. After approximately three cycles, the sensor and silicone reach a steady state and the voltage/strain relationship gains relative consistency. Greyed cycles show upward drift for cycles 8-15, returning to the lower response curve for cycles 16-20, possibly an aliasing effect due to electromagnetic interference.

chamber, with fiber optic leads allowed to hang freely downward within the core.

### C. Pneumatic Control System

Actuation of the soft robot was facilitated using a pneumatic control system to maintain each chamber of the robot at a desired pressure set-point. The control system used pulse-width modulation (PWM) of three SMC VQ100 Series solenoid valves to control airflow from a pressure source into the three chambers of the robot (Fig. 6). The pressure source used was a Parker Hannifin BTC-IIS diaphragm pump connected to a 1-liter bottle acting as a pressure accumulator chamber. The Soft Robotics Toolkit was used as a reference in selecting the aforementioned pump and valve components for the control system [18].

A PID controller was implemented on an Arduino MEGA 2560 microcontroller to modulate the PWM duty cycle of each valve based on the corresponding pressure set-point value and pressure transducer measurement. The control input for each valve was updated at 10 Hz. To reduce pressure oscillations resulting from the binary on-off behavior of the solenoid valves, pneumatic damping was added to the system by placing a segment of 15-inch long, 1/2-inch inner diameter tubing between each valve and its respective pressure chamber. Additionally, pressure transducer data were sampled at 50 Hz and low-pass filtered via a 10<sup>th</sup>-order finite-impulse response (FIR) filter with a cutoff frequency of 5 Hz.

In order to provide a relatively constant pressure source for the valve PWM control system, bang-bang control of the diaphragm pump was implemented on the Arduino, maintaining the accumulator chamber pressure between 6-10 psi. The Arduino microcontroller was also used to read all optical sensors connected inside the robot.

A Python script was used to update pressure set-point values on the Arduino microcontroller for each robot chamber at various time intervals, per a prescribed pressure trajectory matrix. The script also recorded pressure transducer and optical sensor data from the Arduino, along with data from the ATC 3DGuidance trakSTAR electromagnetic (EM) tracker system used to measure the robot’s tip position. All pressure, optical sensor, and EM tracker data were recorded at a 10 Hz sampling frequency.

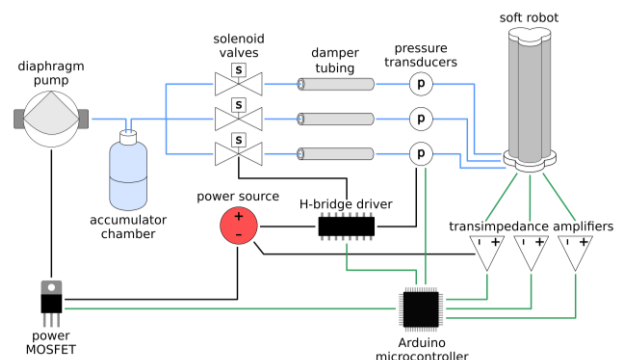


Figure 6. Soft robot pressure controller. Blue lines represent pneumatic connections, green lines represent signal connections, black lines represent power connections.



Figure 7. 45-degree tilt test set-up. EM tracker is inserted in the end cap, optical sensors and pneumatic tubing are connected at base. The EM transmitter is located approximately 10 cm away on a nonmetallic table.

Optical sensor leads were plugged into IR emitter and receiver housings at the base of the robot. The three IR emitters were powered in parallel using an external power supply of 1.4V and 0.24A.

### III. EXPERIMENTAL DESIGN

The objective of these experiments was to demonstrate the utility of the optical sensors in providing an accurate estimate of the pose of the soft continuum robot. Of particular interest were cases in which the robot was undergoing deformation due to external forces, which pressure sensors alone are insufficient to capture. The external forces applied in this work were due to gravitational loading. Gravitational loading—the most basic external disturbance that must be compensated for—is difficult to incorporate into kinematic models in continuum robots, and is frequently a source of errors when estimating spatial positioning [7, 17, 19].

In addition to gravitational loading, we also tested cases where masses were attached to the tip of the continuum robot segment to simulate the presence of one or more additional sections attached serially to create a multi-segment system. For multi-segment soft continuum robots to be controllable, the models used to generate the control inputs have to be able to take into account the effect of weight from distal sections being applied on the base section. They also need to estimate the changes in distal segment behavior due to their tilted orientation on top of the base. The importance of these scenarios, combined with a dearth of accurate modelling solutions for them, suggest that if a sensor were able to capture information about deformations due to gravity (either from being tilted or having a weighted end), establishing this would directly impact its relevance to the field.

Our test set-up involved the pneumatic control system described Section II.C, with pressure transducers and optical sensors connected to an Arduino, which also operated the pressure control valves. The robot segment was placed approximately 10 cm from the EM tracker base, on top of a non-metallic table (to reduce electromagnetic interference). A hollowed, plastic screw (size M5) was inserted into the plastic end-cap of the robot; this provided an insertion location for the EM tracking sensor to monitor the ground-truth location of the robot's tip (Fig. 7).

#### A. Pressure Variation

A set of pressure profiles were generated in to move the end effector in a series of widening circles. Recordings of EM, optical, and pressure sensor data were taken simultaneously via Arduino at a 10Hz frequency. Initial pressures were set to be either 1psi, 2psi, or 3psi, which produced the baseline extension of the soft robot; the initial circle was created by varying the pressure in each chamber sinusoidally with a 0.25psi amplitude, with each chamber at a 120-degree phase offset from the others. After each complete circle, the sinusoid's amplitude increased by 0.25psi, widening the next circle. The test continued until it reached the maximum pressure safety limit of 4psi, or until buckling occurred (generally for tests which started at lower initial pressures, when opposing chambers dropped down to 0psi). Any buckling cases were excluded from the data.

The speed of movement was one 360-degree traversal per minute, a speed slow enough to consider continuously-acquired sensor data to correspond to an approximately static kinetic model. To check this assumption, a separate test with discrete combinations of pressure commands was taken for comparison. There was a 4mm average discrepancy observed between static and slow dynamic EM-tracker coordinates at the same combination of pressures. However, the discrepancy between coordinates on duplicate dynamic tests was 1.5mm apart, likely due to pressure jitter from the PWM valves. The remaining difference is a potential source of error when using the model to predict static postures.

The location of the base of the robot was acquired, also using the EM tracker. This allowed for a coordinate transformation of the EM tracker's ground-truth XYZ

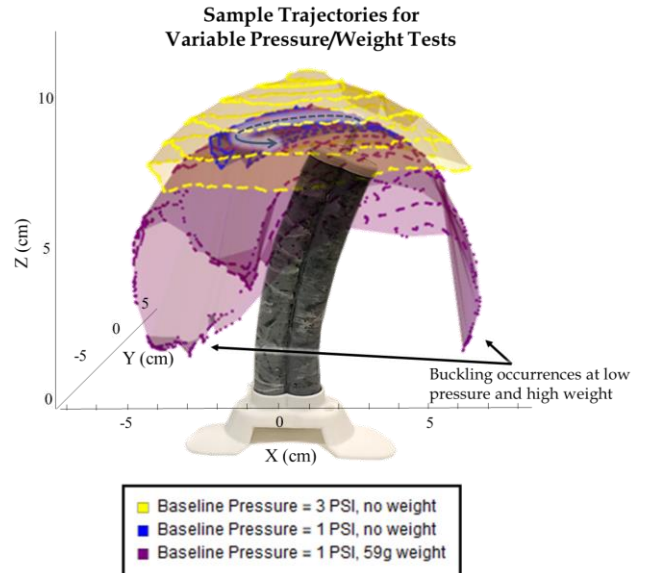


Figure 8. Variation in path trajectory due to baseline pressure and loading of end-effector. The soft robot is initially vertical with equal pressure in all chambers (between 1-3psi). Position, pressure, and optical-sensor data is collected as it moves through a sequence of widening circles; the test end when a max pressure of 4psi is reached (high pressure limit) or buckling occurs (low pressures limit). Higher baseline pressures produce more extension in the robot (yellow trajectory), while weights can induce buckling when two pressurized chambers oppose a single low-pressure chamber.

coordinates into a coordinate frame which was localized to the body of the robot, with the origin at its base (Fig. 8).

### B. End Effector Payload Variation

A similar set of tests was run—with slow, widening circular trajectories and the same set of baseline pressures—but with the additional variable of weights added at the end-effector. The weights used were made from silicone, cast into cylindrical molds, which allowed them to be placed around the screw containing the EM tracker without causing electromagnetic interference (though this was at the cost of reducing the regularity in masses that could be produced). Data was taken with weights of 24.0g and 58.7g. These tests using weight variation were used to supplement the unloaded, 0g weight tests generated in the previous section.

### C. Tilt variation

For the last set of tests, the robot was moved onto a tilting platform. The same circular trajectories were used, with a consistent load weight of 0g and initial pressure of 2psi. The base was then adjusted to tilt away from the EM tracker at angles of 0, 45, and 90-degrees, using acrylic side-plates with slots appropriate for securing the tilt platform at the correct angle. Coordinate transformations were applied as before to create a tilt-invariant frame of reference, localized to the body of the robot (Fig. 9).

### D. Regression Analysis

Regression analysis was conducted to study the significance of the information provided by the optical sensors. Given pressure sensors and/or optical sensors as inputs, kinematic models were trained to predict the soft robot's end-effector position. Two types of model architecture were considered: 1) a linear model and 2) a fully-connected neural network. The linear model serves as a baseline. The neural network was a standard piecewise linear model, comprising two hidden layers connected through ReLU (rectified linear unit) activation functions (Fig. 10). The first hidden layer contains 200 neurons and the second contains 100 neurons; the size of the neural network was

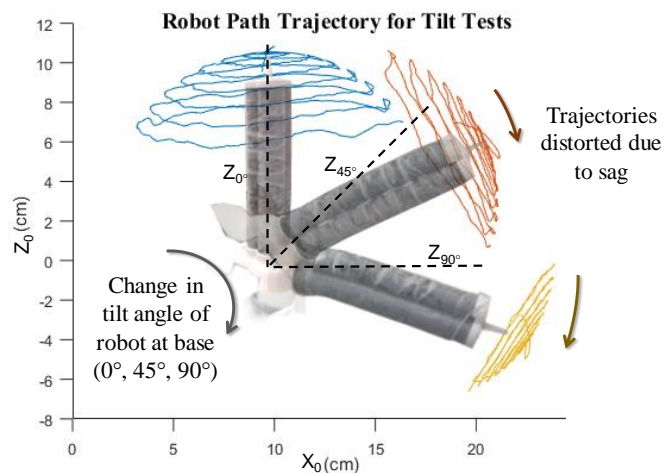


Figure 9. Variation in path trajectory due to tilt, as seen in the frame where the origin is at the base of the robot and the Z-axis extends perpendicular to the base. Gravity causes the end of the robot to sag, leading to the off-center trajectory seen above.

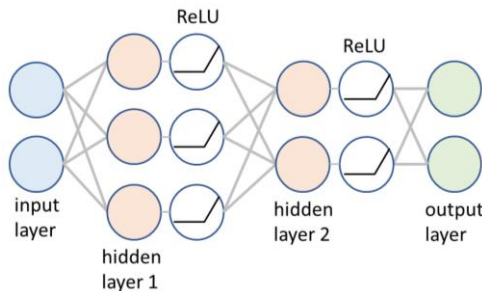


Figure 10. The architecture of the fully-connected neural network

chosen to roughly match the order of the dataset to prevent over or under-fitting.

To validate the performance of each model, a dataset was first sampled without replacement into a training set (90%) and a testing set (10%). Before training, the training set was whitened such that each dimension has zero mean and unit variance. Then each model was trained minimize the square loss on the training set by AdaGrad [20] (implemented in TensorFlow [21]) with minibatch size 128 for 5,000 iterations. Finally, the root-mean-square error (RMSE) on the testing set was computed. This process was repeated 20 times for each dataset and the statistics of testing error are reported. The regression analysis was performed on two datasets. The first dataset was collected in the experiments described Section III-A and Section III-B, containing 24,086 samples and spanning all possible combinations of baseline pressures and weights. The second dataset was collected in the experiments described in Section III-C, containing 12,741 samples with fixed pressure and weight but various tilt angles.

## IV. RESULTS

Tables I and II show the RMSE associated with the linear and neural network models generated, organized by the type of sensors used to inform the model. Table I shows error associated with the model spanning variations in both baseline pressures and weights; Table II shows the error associated with the variable tilt, fixed pressure/weight model. Linear models are used as a baseline comparison for the neural network model; the greatly improved neural network performance is evidence of the underlying nonlinear complexity of the system.

The results suggest that pressure alone is a useful predictor of end-effector position when the tilt angle is zero; predictably, this is especially true for cases in which a large amount of the variation in position is due to modifications in pressure. Supplementing pressure data with optical sensor information does improve the model: in the case containing both pressure and weight variation, accuracy improved from approximately 9mm to less than 2mm along any given axis. Optical sensors on their own showed less predictive value than pressure sensors; this is likely due in part to the sensitivity limits associated with measuring the small changes in strain that occur at lower pressures, particularly with the standard 10-bit ADC resolution of the Arduino.

TABLE I  
ROOT-MEAN-SQUARE ERROR OF PREDICTIVE MODELS WHICH SPAN  
VARIATION IN BOTH PRESSURES AND WEIGHTS

LINEAR MODEL	Optical and Pressure Sensors RMSE	Pressure Sensors RMSE	Optical Sensors RMSE
X (cm)	1.239	1.310	3.022
Y (cm)	1.059	1.384	2.542
Z (cm)	1.509	1.523	1.599

NEURAL NETWORK MODEL	Optical and Pressure Sensors RMSE	Pressure Sensors RMSE	Optical Sensors RMSE
X (cm)	0.241	0.835	1.777
Y (cm)	0.170	0.858	1.418
Z (cm)	0.159	0.967	0.833

Another important contributing factor was variation in baseline optical sensor voltages, most likely due to subtle changes in alignment of fiber optics within the IR emitter and photodiode housings. Close examination of optical sensor data showed that within 7-minute test runs, as well as with many back-to-back tests, optical sensor data was centered around a consistent baseline. However, if housings were jostled between tests or otherwise directly handled, shifts in baseline voltage could result. While the method of securing fiber optic leads was sufficiently sturdy to withstand the natural movement of fiber optics associated with robot motion, future sensors will need to opt for more robust and probably more permanent methods of attachment.

However, for the constant-pressure, variable-tilt test, the optical sensors proved to have much more predictive ability than the pressure sensors. This type of deformation is primarily due to external forces, which can be expected to greatly influence robot shape, yet have a relatively minimal effect on chamber pressures. The combined pressure/optical sensory input again had the greatest predictive ability, reaching an error of close to 2mm again along any given axis.

## V. DISCUSSION

In this work, we outlined the fabrication methods for a novel soft optical sensor which is capable of measuring complex deformation within a soft robot body. Experimental results highlighted several promising aspects of this novel sensing approach, as well as several caveats/disadvantages.

The sensor is capable of measuring strains reliably if prepared properly; that is, with all fiber optic ends securely fastened, and following a “breaking in” period of 2-3 strain cycles. Sensors show a linear response to robot bend angle over the ranges measured, although the magnitude of the voltage response varies between sensors (Fig. 11). It should be noted that in this experiment, optical sensors were placed near the axial center of the robot for convenience of fiber optic routing, an area where strain is minimized. Sensor responsiveness can be expected to improve with more peripheral placement. The soft optical sensor can be attached or even embedded within the soft robot, allowing it to measure actual deformation, which provides advantages over

TABLE II  
ROOT-MEAN-SQUARE ERROR OF PREDICTIVE MODELS WHICH SPAN  
VARIATION IN TILT

LINEAR MODEL	Optical and Pressure Sensors RMSE	Pressure Sensors RMSE	Optical Sensors RMSE
X (cm)	0.702	2.507	1.898
Y (cm)	0.539	0.670	1.101
Z (cm)	0.851	1.011	1.007

NEURAL NETWORK MODEL	Optical and Pressure Sensors RMSE	Pressure Sensors RMSE	Optical Sensors RMSE
X (cm)	0.098	2.517	0.711
Y (cm)	0.072	0.640	0.420
Z (cm)	0.045	0.676	0.283

control-related signals that are unable to capture position errors due to external forces. Our experiments with pressure and optical sensors in a segment of a soft continuum robot show that pressure (i.e. control-related) sensors are unable to capture much important information about the trajectory of even a simple soft robot under the influence of gravity—an undeniably relevant scenario. However, with both pressure and optical sensors, the predictive ability of our kinematic models increased substantially, in some cases even by orders of magnitude. The predictive accuracy of the combined optical/pressure sensors for the pressure/weight NN model is shown in Figure 12.

The soft optical sensors include other advantages, such as resistance to electromagnetic interference, independence of bulky camera or EM-tracker set-ups, and minimal reduction of the soft characteristics of the attached robot. Conceivably, a larger array of sensors could be applied to or embedded within a soft robot body, enabling more detailed characterization of a robot’s configuration. However, for this to be achieved, more work must be done to characterize the behavior of the sensor when undergoing multimodal deformation, as the effects of pressure, bending, and torsion are likely to be coupled with the strain response it is intended to capture. Furthermore, for the sensors to have true predictive

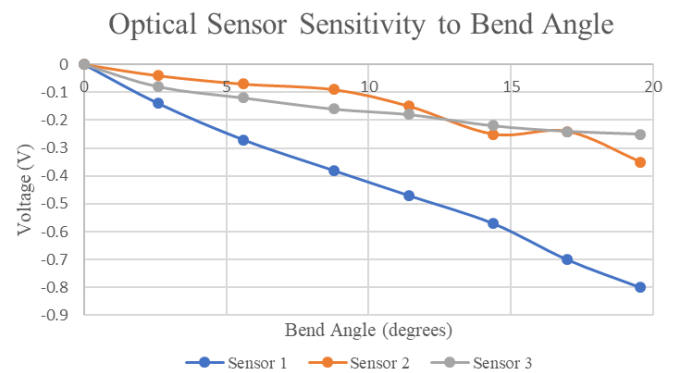


Figure 11. The light attenuation associated with bending the soft robot in the primary direction measured by each sensor. The amount by which each sensor extends falls within its linear range, although sensors are not identically responsive due to variation in the fabrication process and discrete options for manually tuning amplifier gains.

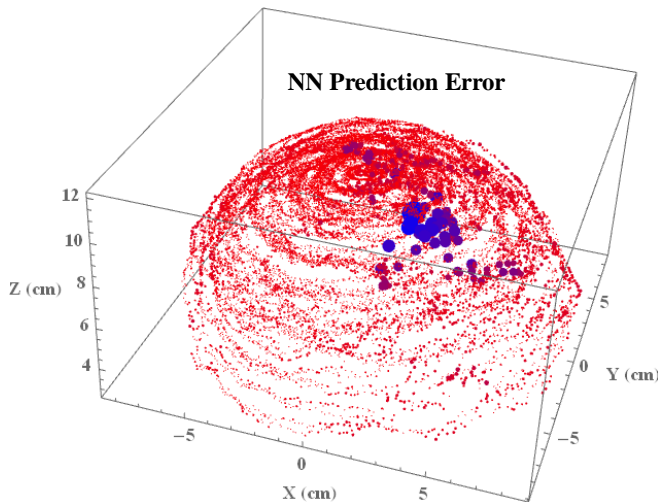


Figure 12. Predicted XYZ coordinates of the end effector in the variable pressure/weight NN model, generated using both pressure and optical sensor inputs. The size and hue of the points shows the spatial error in prediction, where larger/darker points represent greater deviation from actual XYZ coordinates measured by the EM-tracker.

ability, they must be built to require less frequent calibration. This can likely be ensured by using more secure attachments at the photodiode and IR emitter junctions.

## VI. CONCLUSION AND FUTURE WORK

Besides the refinement and full characterization of the soft optical sensors, we see opportunities for greater predictive models where neural networks and extensive sensor networks are combined. Additional sensor/EM-tracker tests would be useful for expanding and refining the pressure-weight-tilt model. Data could also be gathered at faster speeds, to allow generation of dynamic as well as kinematic models. With a larger optical sensor network, it may be possible eventually to remove reliance on pressure sensors, or to predict orientation of the tip in addition to its location in three-dimensional space. (This information would inform the tilt of a subsequent segment, so that an entire soft continuum robot could be modeled). Eventually, we look forward to creating networks that operate in reverse, predicting necessary control signals based off of desired kinematic states despite gravitational perturbations.

## ACKNOWLEDGMENT

This material is based upon work supported by the National Science Foundation under Grant No. 1545287 and NRI award number 1637758. Any opinions, findings, and conclusions or recommendations expressed in this material are those of the author(s) and do not necessarily reflect the views of the National Science Foundation.

## REFERENCES

[1] T. Umedachi, V. Vikas, and B. A. Trimmer, "Highly deformable 3-d printed soft robot generating inching and crawling locomotions with variable friction legs," in *Intelligent Robots and Systems (IROS), 2013 IEEE/RSJ International Conference on*, 2013, pp. 4590-4595: IEEE.

[2] R. F. Shepherd *et al.*, "Multigait soft robot," *Proceedings of the National Academy of Sciences*, vol. 108, no. 51, pp. 20400-20403, 2011.

[3] P. Polygerinos, Z. Wang, K. C. Galloway, R. J. Wood, and C. J. Walsh, "Soft robotic glove for combined assistance and at-home rehabilitation," *Robotics and Autonomous Systems*, vol. 73, pp. 135-143, 2015.

[4] H. In, B. B. Kang, M. Sin, and K.-J. Cho, "Exo-glove: A wearable robot for the hand with a soft tendon routing system," *IEEE Robotics & Automation Magazine*, vol. 22, no. 1, pp. 97-105, 2015.

[5] L. Tiziani, A. Hart, T. Cahoon, F. Wu, H. H. Asada, and F. L. Hammond, "Empirical characterization of modular variable stiffness inflatable structures for supernumerary grasp-assist devices," *The International Journal of Robotics Research*, p. 0278364917714062, 2017.

[6] D. Rus and M. T. Tolley, "Design, fabrication and control of soft robots," *Nature*, vol. 521, no. 7553, pp. 467-75, May 28 2015.

[7] A. D. Marchese, R. K. Katzschmann, and D. Rus, "A recipe for soft fluidic elastomer robots," *Soft Robotics*, vol. 2, no. 1, pp. 7-25, 2015.

[8] Z. Wang, P. Polygerinos, J. T. B. Overvelde, K. C. Galloway, K. Bertoldi, and C. J. Walsh, "Interaction Forces of Soft Fiber Reinforced Bending Actuators," *IEEE/ASME Transactions on Mechatronics*, vol. 22, no. 2, pp. 717-727, 2017.

[9] W. McMahan *et al.*, "Field trials and testing of the OctArm continuum manipulator," in *Robotics and Automation, 2006. ICRA 2006. Proceedings 2006 IEEE International Conference on*, 2006, pp. 2336-2341: IEEE.

[10] H. Wang, W. Chen, X. Yu, T. Deng, X. Wang, and R. Pfeifer, "Visual servo control of cable-driven soft robotic manipulator," in *Intelligent Robots and Systems (IROS), 2013 IEEE/RSJ International Conference on*, 2013, pp. 57-62: IEEE.

[11] P. Yong-Lae, C. Bor-Rong, and R. J. Wood, "Design and Fabrication of Soft Artificial Skin Using Embedded Microchannels and Liquid Conductors," *IEEE Sensors Journal*, vol. 12, no. 8, pp. 2711-2718, 2012.

[12] L. Jiang, K. Low, J. Costa, R. J. Black, and P. Yong-Lae, "Fiber Optically Sensorized Multi-fingered Robotic Hand," *IEEE International Conference on Intelligent Robots and Systems (IROS)*, 2015.

[13] S. Sareh, Y. Noh, M. Li, T. Ranzani, H. Liu, and K. Althoefer, "Macrobend optical sensing for pose measurement in soft robot arms," *Smart Materials and Structures*, vol. 24, no. 12, p. 125024, 2015.

[14] H. Zhao, K. O'Brien, S. Li, and R. F. Shepherd, "Optoelectronically innervated soft prosthetic hand via stretchable optical waveguides," *Science Robotics*, vol. 1, no. 1, p. eaai7529, 2016.

[15] C. To, T. L. Hellebrekers, and Y.-L. Park, "Highly stretchable optical sensors for pressure, strain, and curvature measurement," in *Intelligent Robots and Systems (IROS), 2015 IEEE/RSJ International Conference on*, 2015, pp. 5898-5903: IEEE.

[16] F. Caralt, J. Molnar, T. Cahoon, J. Stingel, and F. L. Hammond, "Diffusion-Based Optical Sensors for Multimodal Strain Measurement in Soft Devices," presented at the IEEE Sensor Conference, Glasgow, Scotland, UK, 2017.

[17] R. J. Webster and B. A. Jones, "Design and Kinematic Modeling of Constant Curvature Continuum Robots: A Review," *The International Journal of Robotics Research*, vol. 29, no. 13, pp. 1661-1683, 2010.

[18] D. P. Holland, E. J. Park, P. Polygerinos, G. J. Bennett, and C. J. Walsh, "The soft robotics toolkit: shared resources for research and design," *Soft Robotics*, vol. 1, no. 3, pp. 224-230, 2014.

[19] A. D. Marchese, R. Tedrake, and D. Rus, "Dynamics and trajectory optimization for a soft spatial fluidic elastomer manipulator," *International Journal of Robotics Research*, vol. 35, no. 8, 2015.

[20] J. Duchi, E. Hazan, and Y. Singer, "Adaptive subgradient methods for online learning and stochastic optimization," *Journal of Machine Learning Research*, no. Jun 12, pp. 2121-2159, 2011.

[21] M. Abadi, *et al.*, "Tensorflow: Large-scale machine learning on heterogeneous distributed systems," *arXiv*, vol. 1603.04467, 2016.